Effect of Modifiers on the Microstructure of Rapidly Solidified AlSi10Mg Alloy

SILVIA MAROLA, GIANLUCA FIORE, and LIVIO BATTEZZATI

In this work, melt-spun ribbons of AlSi10Mg added with modifiers (Er, Sr, or nano-TiB$_2$) were produced to investigate the combined effect of modification and rapid solidification on eutectic Si. The resulting eutectic microstructures are more isotropic in comparison to that of the base alloy affecting the mechanical properties of the alloys. The modification of Si morphology and supersaturation caused by the modifiers were investigated by microscopy, X-ray diffraction, and differential scanning calorimetry. Compared to melt-spun AlSi10Mg, the eutectic Si network is finer and less continuous when Er or Sr is added, and disrupted with rounded crystals dispersed in the matrix when adding nano-TiB$_2$. The level of supersaturation decreases in the order Er–nano-TiB$_2$–Sr. A transition from columnar Al grains at the wheel side to finer equiaxed grains at the air side was found in the unmodified ribbon and in the one containing nano-TiB$_2$ by means of electron backscattered diffraction. The Er- and Sr-modified ribbons display equiaxed Al grains of constant size throughout their thickness. The average hardness obtained by nano-indentation tests was lower than that of AlSi10Mg. The less continuous Si network causes the hardness drop but provides more isotropic mechanical properties.

I. INTRODUCTION

IN the last 40 years, extensive research activities provided basic understanding of the main phenomena occurring during rapid solidification, RS.[1–4] RS resulted mainly from the solidification of fine droplets,[5] melt spinning (MS) of continuous or discontinuous ribbons,[6,7] or *in situ* melting and solidification of thin surface layers.[8] With the advent of additive manufacturing (AM), the production of bulk components of rapidly solidified alloys has become possible.

Increasing the cooling rate is appealing from a metallurgical point of view. Nucleation can be depressed to temperatures far below the *liquidus* moving toward non-equilibrium solidification on undercooling. Novel microstructures are found due to the extension of solid solubility, the occurrence of microcrystalline structures and metastable phases.[9]

In metal AM, 3D objects are built with high cooling rates leading to microstructural refinement and extended solid solubility.[10–13] It is well known that mechanical properties are affected by the microstructural features developed in the process.[9] For instance, Al–Si alloys processed by AM possess higher yield strength and lower ductility than the cast counterpart and display substantial increase in hardness.[14,15] They contain a fine cellular structure of supersaturated Al-rich phase with Si at the cell boundaries. This strengthens the material thanks to dislocations pile-up at grain boundaries and their resistance to slip transfer. Changing the Si distribution in the sample by means of thermal treatment of the built samples allows tuning the mechanical properties for the final application.[14,15]

Epitaxial growth is one of the most common features of metal AM. It results in columnar grains along the building direction and often causes anisotropic mechanical properties with an increase in hot cracking tendency.[16,17] This is one of the main reasons for the poor processability of the most widespread high-strength Al alloys. To tackle this issue, inspiration was taken from the conventional practice in Al–Si casting of inoculation/modification.[18–21] Adding inoculants to the melt promotes heterogeneous nucleation of primary phases thus originating more isotropic grain structures. Modifiers, instead, influence the eutectic morphology by altering the nucleation and growth mechanism of phases in the interdendritic zones. These additions may improve both the processability and mechanical

SILVIA MAROLA is with the Dipartimento di Meccanica, Politecnico di Milano, Via La Masa, 20156, Milan, Italy and with the Istituto Italiano di Tecnologia (IIT), Center for Sustainable Future Technologies, Via Livorno 60, 10144 Turin, Italy and also with the Dipartimento di Chimica, Università di Torino, Via Pietro Giuria 7, 10125 Turin, Italy. Contact e-mail: silvia.marola@polimi.it GIANLUCA FIORE and LIVIO BATTEZZATI are with the Dipartimento di Chimica, Università di Torino.

properties of the alloys. For this reason, in the last years, a line of research in AM was focused on modifying Al alloys by means of grain refiners to change the grain structure from columnar to equiaxed. Modification was successfully attempted by several research groups. Belelli *et al*. obtained an equiaxed EN AW 2618 exploiting the inoculation potency of TiB$_2$.[22] Martin *et al*. successfully demonstrated that the increased nucleation provided by small quantities of grain refiners allows to process successfully the 7075 and 6061 aluminum alloys making them suitable for AM.[16]

As demonstrated in previous studies, the cooling rates needed to produce MS ribbons may correspond to those occurring when processing the same alloy by AM. Results on microstructure, supersaturation, and precipitation in melt-spun samples can be correlated to those obtained by AM. A difference in supersaturation was found in AM and MS samples due to the varied mechanism of heat transfer in the two processing routes. In powder bed AM, the intimate contact between the melt pool and the substrate provides highly effective heat dissipation as well as solid-state quenching. In MS, the detachment of the ribbons from the quenching medium leads to reduced heat transfer and self-annealing. The recalescence effect occurring in melt-spun samples is thus responsible for the decreased supersaturation. Nevertheless, the microstructural features at the air side of MS ribbons together with results obtained from solidification modeling indicated a similar cooling rate between AM and MS, allowing for the use of MS for testing new compositions for AM processes.[11,23]

Along this line of thought, this work aims to investigate how modifiers (specifically Er, Sr, and nano-TiB$_2$) affect the microstructure and eutectic morphology of AlSi10Mg, an Al alloy of widespread use in AM. The Er was selected for modification because multiple effects were reported in cast and RS materials: the refinement of eutectic Si, the occurrence of fine Al–Al$_3$Er eutectic, and the precipitation of semi-coherent Al$_3$Er strengthening particles.[24–26] The Sr was selected because it is a conventional eutectic modifier of cast Al alloys generally employed for improving mechanical properties.[27–29] Nano-TiB$_2$ was selected because the compound is one of the main inoculants employed for Al alloys and has strong effect on both the eutectic and the primary phase of cast Al alloys.[20,30,31] Moreover, TiB$_2$ was proven to act as reinforcing agent in composites to improve the mechanical properties of the alloys.[32] The aim of the work is to determine if these additives can promote the modification of the eutectic Si network in RS with the final goal of obtaining more isotropic mechanical properties reducing the need for subsequent post-processing.

II. MATERIALS AND METHODS

A. *Samples Production*

The production of modified samples occurred in different ways according to the selected additive: Erbium (Er), Strontium (Sr), and nano-TiB$_2$. All were added to the base AlSi10Mg alloy to reach approximately 0.05 at. pct in modifier content. 0.3 wt pct Er was added to the AlSi10Mg powder (EOS GmbH) as Al3Er gas atomized powder (Nanoval GmbH), and the powders were homogenized by mechanical mixing. 0.1 wt pct nano-TiB$_2$ (US Research Nanomaterials, Inc.) was added in the form of powder to the AlSi10Mg powder and mechanically mixed. An Al10Sr master alloy was produced by arc melting starting from chemically pure Al and Sr. Flakes of the Al10Sr alloy appropriate to obtain the amount of 0.1 wt% Srr was then mixed with the AlSi10Mg powder, and gently pressed to form pellets. The mixture was finally arc melted.

All the modified alloys were employed to produce samples by MS by ejecting the molten alloy onto a Cu wheel rotating at 10 m/s. All MS ribbons were 110 ± 35 μm in thickness and 5 to 8 mm in width.

B. *Microscopy and EBSD*

Samples were analyzed by means of field emission scanning electron microscope (FESEM) and electron backscattered diffraction (EBSD) to investigate the microstructural features and the α-Al grain orientation and morphology after modification and RS, respectively. For microscopy, samples were embedded in resin, mechanically ground, and finished down to 40 nm using colloidal silica. The microstructure was revealed by etching the samples for 5 seconds using a 0.5 pct HF solution. A Zeiss SUPRA™ 40 FESEM was employed to get secondary electron imaging. EBSD inverse pole figure (IPF) maps were acquired on the cross-section of ribbons polished down to 40 nm using a FIB-FESEM/EBSD/TOF–SIMS Tescan S9000G microscope.

C. *X-Ray Diffraction (XRD)*

XRD measurements were made with a PANalytical X'Pert PRO diffractometer in Bragg–Brentano configuration using the K$_{\alpha}$ emission line of a Cu filament (λ_{Cu} = 1.5418 Å) for phase identification. Patterns were acquired in the 2θ range from 20 to 140 deg at steps of 0.0167 deg. Rietveld refinement was carried out on the XRD patterns using the MAUD software to determine Al lattice parameter, the percentage of Si in the alloy, and the dimension of the Si crystallites.

D. *Differential Scanning Calorimetry (DSC)*

A TA Q100 DSC was used to detect precipitation phenomena from the supersaturated matrix and changes in the melting and solidification temperatures. For investigation of precipitation phenomena use was made of aluminum crucibles at the heating rate of 20 °C/min in the temperature range from 50 °C to 450 °C, equilibrating the heat flux for 15 minutes at each temperature. Scans to monitor the melting and solidification of the alloy were performed in alumina crucibles up to 700 °C and back at the same heating/cooling rate. The appropriate instrumental calibrations were performed for the two sets of crucibles.

E. Nano-indentation

Nano-indentation tests were performed using a Tri-boindenter 950 (TI950) equipped with a Berkovich tip. Indentation was performed every 4 μm according to a grid pattern having width of 40 μm and variable length according to the specimen thickness. The load velocity was 100 μN/s; the maximum load was fixed to 2.5 mN and kept for 5 seconds. Loading and un-loading were made at the same velocity.

III. RESULTS AND DISCUSSION

The DSC traces related to the melting of the alloys were employed as a control parameter to evaluate the quality of the ribbons.

Three overlapped melting events are distinguished for all samples (Figure 1). The first minor signal (inset of Figure 1) occurring approximately at 560 °C is attributed to melting reactions involving minority phases present in the alloys. Its absence in the Sr-containing sample is probably related to the loss of Mg due to its evaporation during arc melting because of its low boiling point of 1091 °C. The second and main melting event occurs at approximately 570 ± 3 °C, in agreement with the eutectic temperature of the Al–Si alloys. Sometimes, the eutectic melting displays several minima deriving from the superposition of the melting signal of different pieces of ribbons. The third signal appears as a shoulder of the main one at higher temperature (590 °C) and is related to the melting of the primary Al phase, in general agreement with the *liquidus* temperature of the binary Al–Si phase diagram except for the ribbon modified with Er for which the signal ends at higher offset temperature. Since all modifiers are added in atomic concentrations below 500 ppm and the melting temperatures are all close to each other, it is impossible to distinguish the melting of the ternary eutectics
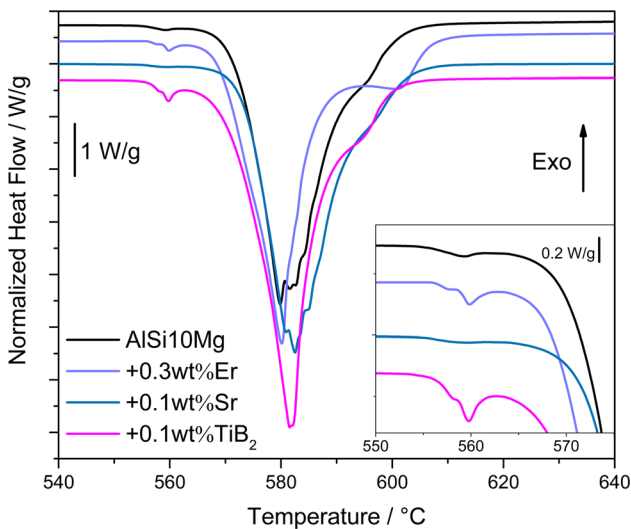
containing Er, Sr, and Ti in the DSC curves. In the Er-, Sr-, and nano-TiB$_2$-containing alloys, the primary phase is always the α-Al, as demonstrated by the ternary phase diagrams assessed in the literature.[33–35] The enthalpies of melting of the unmodified AlSi10Mg alloy and the alloys containing Er and Sr agree within the scatter of data, while the sample modified with nano-TiB$_2$ has higher melting enthalpy. The DSC onset and offset temperatures and the enthalpies of melting and solidification are reported in Table I. A second scan confirms the sequence and heat content of the melting signals. Therefore, the alloys appear homogeneous.

Figure 2 reports images of the cross-sections of AlSi10Mg and Er-, Sr-, or nano-TiB$_2$-containing ribbons. As already discussed in Reference 11, the unmodified AlSi10Mg ribbon displays the zone A–B microstructure typical of rapidly solidified crystalline alloys. The microstructure is featureless at the wheel side (bottom of Figures 2(a) and (b)) and becomes cellular with the α-Al primary phase surrounded by fibrous eutectic toward the air side (top of Figures 2(a) and (c)). Zone A solidified at high undercooling, whereas zone B experienced less undercooling. In fact, during the first stage of solidification, the heat subtraction occurs through the Cu wheel of the apparatus, while the solidification conditions change with heat dissipation in the atmosphere once the ribbon detaches from the wheel leading to the formation of equiaxed grains.[36] On the air side, the eutectic Si network is continuous around the cells, and lamellar eutectic is seen in some areas (Figure 2(c)). On the wheel side, fine Si precipitates are homogeneously distributed inside the Al matrix (Figure 2(b)). They are due to Si precipitation from the supersaturated Al primary phase. All modified samples have different microstructures with respect to the base alloy. The one containing 0.1 wt pct Sr is the most similar to AlSi10Mg having microstructure composed of α-Al cells surrounded by fine Si eutectic (Figures 2(g) through (i)). Here, a featureless microstructure is no longer found at the wheel side, but the microstructure is finer for a few microns at both the wheel and air side (Figures 2(h) and (i)). At higher magnification (Figure 2(i)), it is observed that the eutectic Si network around the primary phase is less continuous in comparison to the AlSi10Mg ribbon. The absence of the featureless microstructure on the wheel side and the rupture of the eutectic Si network are even more apparent in the ribbons modified with Er (Figures 2(d) through (f)) and nano-TiB$_2$ (Figures 2(j) through (l)). Both cross-sections show uniform microstructures: in the ribbon containing 0.3 wt pct Er, Al cells are clearly distinguished (Figures 2(e) and (f)), whereas in the alloy containing 0.1 wt pct nano-TiB$_2$, Al cells are more open with Si crystals segregated in discontinuous strips (Figures 2(k) and (l)). The segregation of Si in the nano-TiB$_2$-containing ribbon is evident at the wheel side (Figure 2(l)), where Si crystals appear aligned along the direction of heat subtraction perpendicular with respect to the cross-section of the ribbon. The fact that there is no strong microstructural difference between the wheel and air side in the ribbons containing modifiers suggests that

Fig. 1—Melting curves of the AlSi10Mg and AlSi10Mg containing Er, Sr, and nano-TiB$_2$ melt-spun ribbons. The inset represents an enlargement of the curves displaying the first small melting signal.

inoculants limit the undercooling for the crystallization of α-Al already on the wheel side.

As apparent in Figure 2, eutectic Si is thinner and more fragmented in comparison to the base alloy because of modification by Er and Sr. Moreover, increased roundness of Si particles is seen in the Er-containing alloy. The thickness of Si fibers, determined by means of careful image analysis, varies from 125 ± 44 nm in the base alloy to 174 ± 41 nm and 114 ± 25 nm in the alloys modified with Er and Sr, respectively. Since Si fibers in the Sr-modified alloy have approximately the same thickness of those of the base alloy, even though the network is less continuous, it is deduced that the modification with Sr results in a more frequent Si nucleation, as suggested by Liao et al.,[37] without changes in the growth process. When the alloy is modified with nano-TiB_2, Si fibers are fragmented and coarser having thickness of 229 ± 64 nm. It is thought that this stems from the combined effects of RS and inoculation: in fact, the shape of crystals is known to depend on growth mode. At higher temperature (less undercooling with respect to a similar *liquidus*), growth is faster and less faceted. The solidification is led by the α-Al phase that eventually engulfs the eutectic at limited or no undercooling forming therefore larger Si crystals mostly homogeneously distributed in the matrix.[38]

The effect of the three modifiers on the spatial and crystallographic orientation of the α-Al grains was verified using EBSD; a comparison of the results is reported in Figure 3. There is no overall crystallographic orientation in the ribbons, but there is difference in the shape of Al grains moving from the wheel side to the air side when changing the chemical composition of the alloy. It is crucial to underline that the grains identified with EBSD do not correspond to the cells of primary phase visible in Figure 2. Each α-Al grain contains some of the primary Al cells surrounded by eutectic Si as deduced from the scale of the microstructures in Figures 2 and 3. The IPF map of the unmodified ribbon (Figure 3(a)) shows a transition from columnar Al grains at the wheel side to equiaxed Al grains at the air side. Even more pronounced columnar grains were observed at the wheel side of ribbon containing nano-TiB_2, Figure 3(d). On the contrary, the Er- and Sr-containing ribbons display equiaxed grain structure throughout their thickness (Figures 3(b) and (c), respectively), thus indicating an effect on Al nucleation. Where present, columnar grains were observed to be tens of microns long, while equiaxed grains have diameters of approximately 5 μm. These results (Table II) were obtained by measuring the α-Al grain size with the intercept method. Since some ribbons show columnar to equiaxed transition at approximately half their thickness, the intercept method was applied by drawing both vertical and horizontal intercepts on both halves of the sections of the ribbons to obtain the local grain size.

The size of the Al grains is approximately the same in both directions for all the samples on the air side, with a slight increase compared to AlSi10Mg, indicating that the α-Al nucleation frequency is similar in all ribbons. Conversely, at the wheel side, the grain size is reproduced along the horizontal direction, but changes in the

vertical one in the case of the ribbon containing nano-TiB_2. In this case, the dimension of the α-Al grains is approximately double with respect to that found for the other zones of the samples. Therefore, it appears that TiB_2 does not effectively nucleate the Al in the present working conditions. However, in the ribbon containing nano-TiB_2 after initial columnar growth in contact with the heat sink, the solidification conditions change possibly because of the effect of recalescence due to release of latent heat, as previously described for AlSi10Mg. The inability of nano-TiB_2 to act as α-Al nucleation agent can be justified considering the literature findings on the poisoning effect of the grain refinement efficiency of TiB_2 arising from the interaction between TiB_2, $TiAl_3$, and solute Si. The TiB_2 surface was reported in literature to be energetically favorable for the attachment of Si atoms, resulting in the formation of a surface layer of titanium silicide that negatively affects the nucleation potency of the boride.[39,40] The poisoning of the TiB_2/$TiAl_3$ nucleation sites with Si is supported by the Si crystals distribution at the wheel side of the ribbon modified with nano-TiB_2. The arrangement of Si in rows perpendicular to the cross-section of the ribbon (see the micrograph in Figure 2(k)) at the wheel side in correspondence with the Al columns (see the IPF map in Figure 3(d)) could indicate that the titanium-rich particles are rejected by the primary Al together with the Si during the first stage of solidification acting in turn as heterogeneous nucleation sites for the Si crystals.

XRD measurements confirm the phases present after solidification and provide measure of the level of solute Si which was quantified by Rietveld refinement of patterns. Figure 4(a) compares the XRD patterns acquired on the air side of all ribbons. All samples display the same phases, face centered cubic (fcc) Al (reference pattern 00-004-0787), and diamond cubic Si (reference pattern 00-027-1402). No other reflections were identified, as the amount of phases possibly produced by modifying elements added to the AlSi10Mg alloy is under the detection limit of the XRD technique.

On the air side of all modified samples, the patterns show slight (111) texture, visible at 38.5 deg, while the air side of the unmodified alloy shows a (200) texture at 44.7 deg. The wheel side of the modified samples does not show texture, whereas a (111) preferential orientation is observed for AlSi10Mg. The lack of textures at the wheel side of the ribbon containing nano-TiB_2 indicates that the Al columns are randomly oriented, contrary to what was observed for the unmodified alloy. Together with the findings on the spatial distribution of Al grains reported in the previous paragraph, these findings confirm the well-known structural diversity occurring in melt-spun Al–Si alloys, at least in the case of the unmodified alloy.[41,42] From Figure 4(b) reporting the angular position of the (111) reflection of Si and the quantification of Si obtained by Rietveld refinement (Table III), it is evident that the RS resulted in Si supersaturation and that the extension of solid solubility varies according to the sample considered. The unmodified AlSi10Mg alloy has the lowest quantity of free-Si and, therefore, the highest supersaturation. In the

Table I. Melting and Solidification Onset and Offset Temperatures and the Relative Enthalpies for the AlSi10Mg Alloy and for the Alloys Modified with 0.3 Wt Pct Er, 0.1 Wt Pct Sr, and 0.1 Wt Pct Nano-TiB$_2$

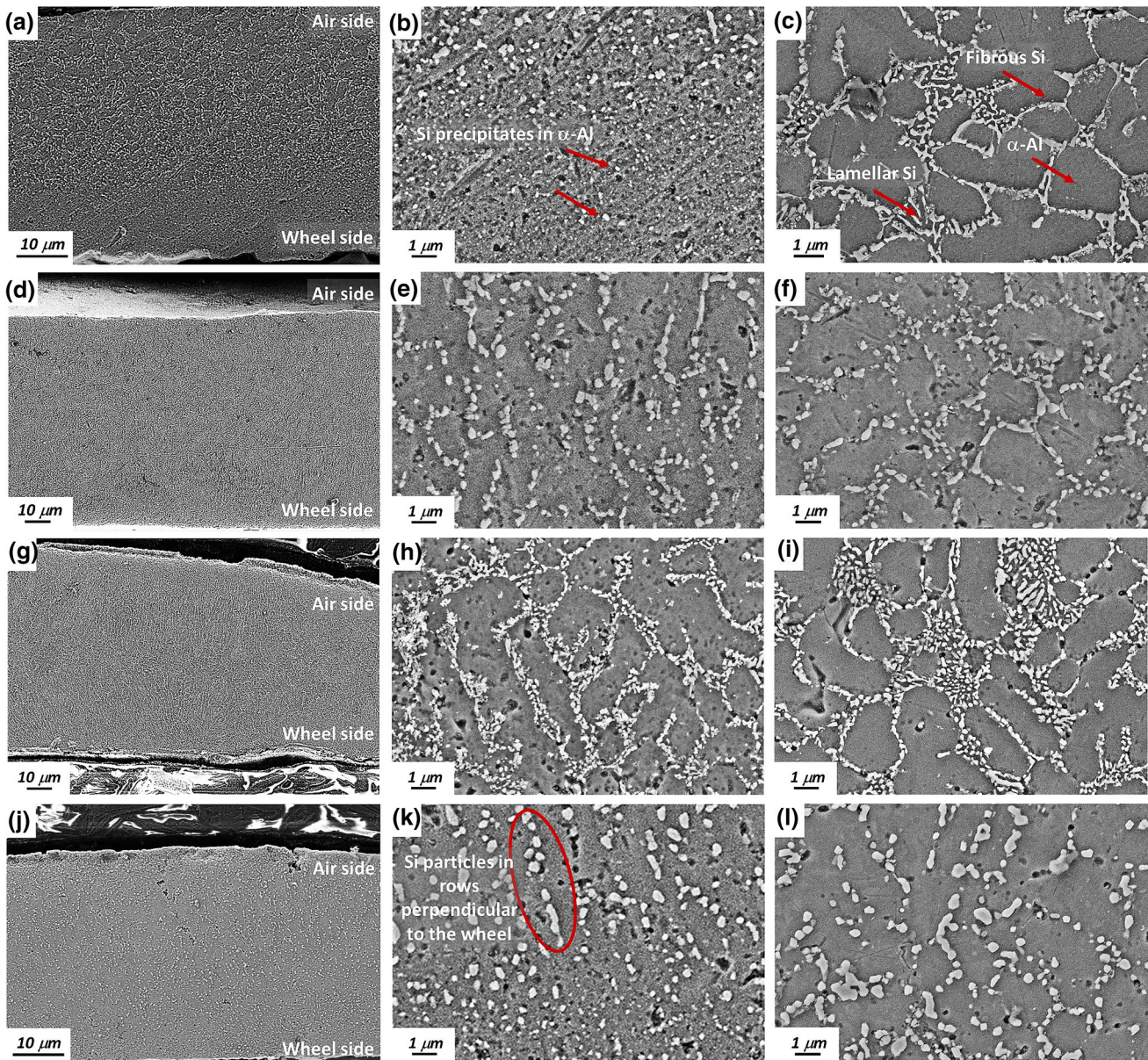|	T_{onset} (°C) Melting	T_{offset} (°C) Melting	ΔH_{melt} (J/g)	T_{onset} (°C) Solidification	T_{offset} (°C) Solidification	ΔH_{sol} (J/g)
AlSi10Mg	571 ± 1	603 ± 1	458 ± 12	577 ± 6	552 ± 1	449 ± 1
AlSi10Mg + Er	568 ± 1	609 ± 3	449 ± 11	587 ± 1	550 ± 1	447 ± 2
AlSi10Mg + Sr	573 ± 1	603 ± 1	463 ± 8	587 ± 1	551 ± 1	459 ± 1
AlSi10Mg + TiB$_2$	569 ± 1	602 ± 3	495 ± 7	584 ± 1	549 ± 1	483 ± 3

Fig. 2—Micrographs of the melt-spun unmodified and modified ribbons with the addition of inoculants. (*a*) through (*c*) refer to the AlSi10Mg alloy, (*d*) through (*f*) to the ribbon containing 0.3 wt pct Er, (*g*) through (*i*) to the ribbon modified with 0.1 wt pct Sr, and (*j*) through (*l*) to the ribbon containing 0.1 wt pct nano-TiB$_2$. In particular, the micrographs in (a), (d), (g), and (h) represent the complete cross-section of the ribbons. Those in (b), (e), (h), and (k) refer to the wheel side of the ribbons and, finally, those in (c), (f), (i), and (l) refer to the air side of the ribbons.
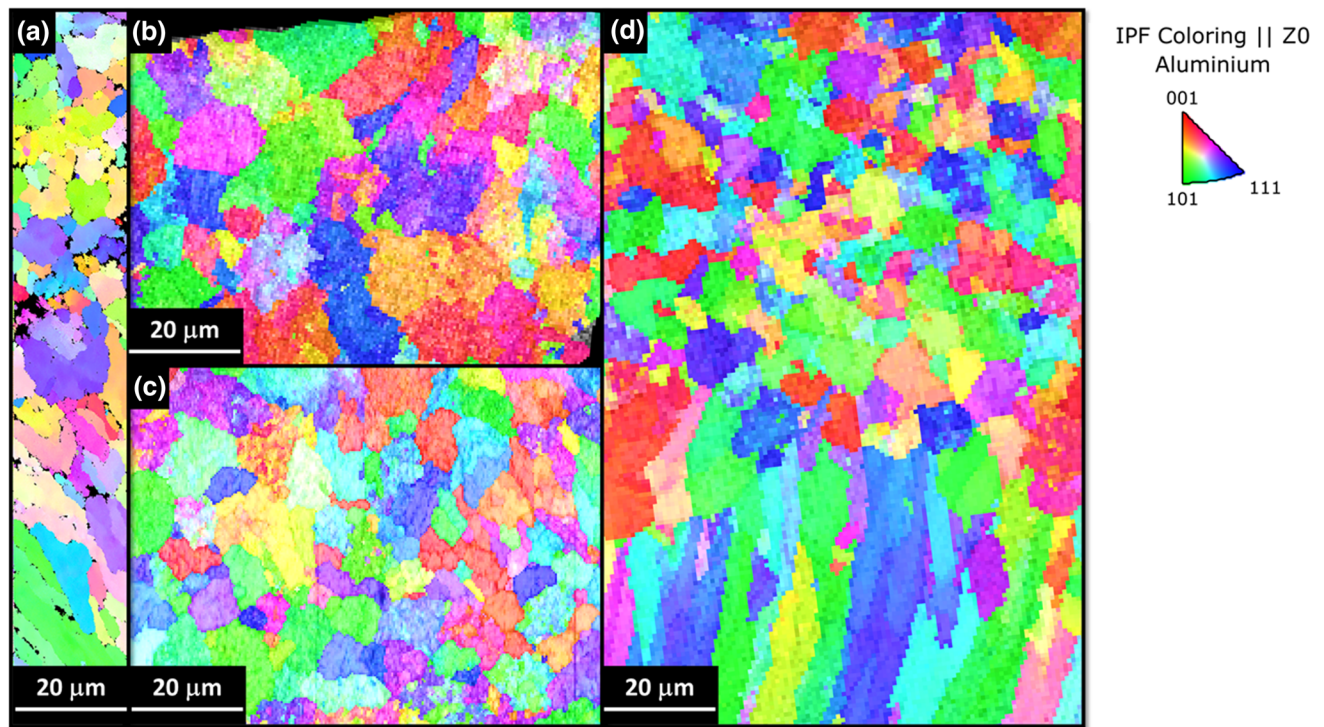
Fig. 3—EBSD IPF maps of AlSi10Mg (*a*), AlSi10Mg + Er (*b*), AlSi10Mg + Sr (*c*), and AlSi10Mg + TiB$_2$ (*d*). The wheel side is at the bottom of the image, while the air side is at the top.

modified ribbons, Si supersaturation was found to follow the order AlSi10Mg + Er > AlSi10Mg + nano-TiB$_2$ > AlSi10Mg + Sr. The dimension of the Si scattering domains was also determined by Rietveld refinement. As it appears from Table III, Si crystallites are smaller in the unmodified and in the alloy containing Sr, even though, from a microstructural point of view, these two ribbons display more continuous fibrous eutectic structure. This suggests that Si is frequently re-nucleated in these alloys. The decreased supersaturation in the Sr-modified alloy, moreover, may derive from increased Si nucleation resulting in an overall reduction in crystallite dimension. In the ribbons modified with Er and nano-TiB$_2$, Si crystallites are considerably larger suggesting that those seen in the microstructure are single crystals. The high supersaturation of the ribbon modified with Er, similar to that of AlSi10Mg, and the presence of larger Si crystallites suggest that the addition of Er results in a decreased nucleation frequency of eutectic Si due to a poisoning interaction between Er and the impurities of the alloy.[25]

These results show that all modifiers affect the nucleation of eutectic Si and, thus, its size and morphology. It is assumed that in all the modified ribbons, Si nucleates heterogeneously and with varied frequencies on some impurity of the AlSi10Mg alloy. In particular, a higher nucleation frequency is observed for the Sr-containing alloy, while the alloy containing Er possesses a lower one due to its poisoning of the Si nucleants. In the nano-TiB$_2$-modified ribbon, the topology of the eutectic changes, indicating that the solidification is led by the Al.[43]

The number and size of Al and Si crystals point to an effect on nucleation of phases of the modifiers employed in this work, whereas the shape of eutectic Si indicates an effect on growth during solidification. The present data do not allow further insight onto the mechanism of nucleation and growth which have been recently reviewed for conventional casting,[43] *i.e.*, whether ternary phases such as Al$_2$Si$_2$Sr[43] or Al$_3$Si$_2$Er$_2$[33] have a specific role on either process.

DSC measurements were carried out to confirm the Si supersaturation level upon alloy modification. A comparison of the precipitation curves obtained in DSC is reported in Figure 5(a).

Except for the alloy containing Sr, all samples display two precipitation signals: the first being more intense and occurring at different temperatures, while the second occurs in the same temperature range. These signals are of the same type described for the AlSi10Mg alloy in Reference 11 and are associated to the precipitation of Si and Mg compounds plus other impurities, respectively. The absence of the second precipitation signal in the alloy containing Sr is likely associated to the selective evaporation of Mg during the arc melting of the alloy before RS. The onset temperature and the enthalpy of the Si precipitation signal are indicative of Si supersaturation in the samples: the higher the temperature and the lower the enthalpy, the lower the amount of Si retained in the solid solution.[11] From Figure 5(a), it is apparent that in all modified ribbons, Si precipitation occurs at slightly higher temperature and implies lower enthalpy indicating reduced Si supersaturation and possibly reduced number of quenched vacancies

Table II. Al Grain Dimensions of the Unmodified and Modified Alloys Obtained by Applying the Intercept Method

			AlSi10Mg	AlSi10Mg + Er	AlSi10Mg + Sr	AlSi10Mg + TiB$_2$
Al Grain Size (μm)	horizontal intercepts	air side	3 ± 1	5 ± 1	5 ± 2	5 ± 1
		wheel side	6 ± 2	6 ± 1	5 ± 1	5 ± 1
	vertical intercepts	air side	4 ± 1	7 ± 2	6 ± 1	6 ± 1
		wheel side	5 ± 1	6 ± 2	7 ± 1	14 ± 1

Grain dimensions are reported separating wheel and air sides and considering horizontal and vertical intercepts.
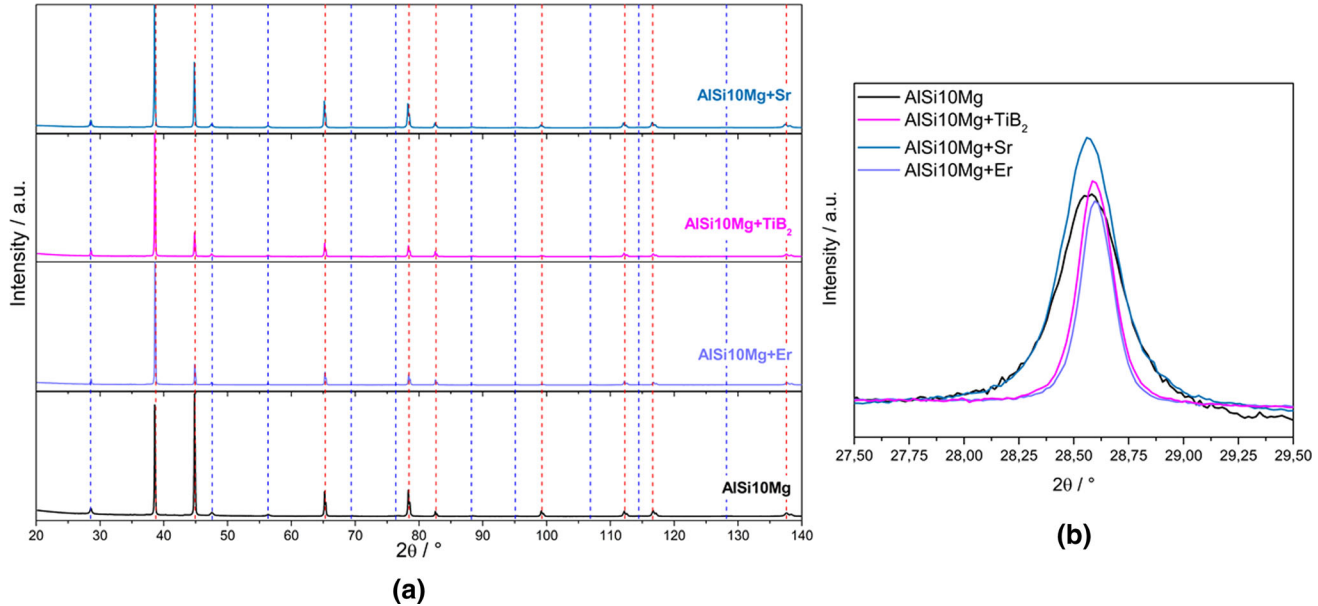
Fig. 4—XRD patterns of the air side of both unmodified and modified ribbons, the dashed blue lines represent diamond cubic Si reflections, while the dashed red lines represent fcc Al reflections (*a*). Enlargement on the (111) reflection of Si (*b*) (Color figure online).

Table III. Comparison of Si Content and Dimension of Si Crystallites in the AlSi10Mg, AlSi10Mg + Er, AlSi10Mg + Sr, and AlSi10Mg + TiB$_2$ Ribbons

	AlSi10Mg	AlSi10Mg + Er	AlSi10Mg + Sr	AlSi10Mg + TiB$_2$
Si Content (Wt Pct)	5.7 ± 0.4	5.9 ± 0.8	8.6 ± 0.3	8 ± 1
Dimension of Si Crystallites (nm)	42 ± 5	224 ± 25	60 ± 4	208 ± 28

with respect to the AlSi10Mg ribbon.[44,45] Accounting for the DSC curves, the ribbon containing Sr displays the lowest supersaturation (Table IV), confirming the results obtained from the Rietveld refinement of the XRD patterns (Table III). This can be explained considering that, as reported in literature,[29,46,47] Sr causes the eutectic Si to nucleate heterogeneously at larger undercooling in the interdendritic liquid resulting in the formation of more Si nuclei restricted in growth.[43] Due to the presence of Sr, Si nucleates with increased frequency, but its growth temperature is reduced: therefore, smaller crystallites are formed and consequently the level of supersaturation is reduced, as apparent also from the morphology of Si fibers and the results obtained by XRD.

The effect of the alloy modification on the solidification at a low rate was also studied by DSC (Figure 5(b)). Table I reports the results on both onset and offset temperatures as the solidification enthalpies. The solidification temperature is higher for the modified ribbons confirming their ability to promote the nucleation of α-Al at higher temperatures, as also found for the Er-addition to a similar alloy.[25] This effect is the same for all the compositions under study. In the sample containing nano-TiB$_2$, a higher melting and solidification enthalpy was noticed. It is due mostly to the minor peaks before the main melting events and at the end of solidification. For all the modified alloys, a shift toward lower temperature of the Si eutectic was observed (Figure 5(b)) confirming
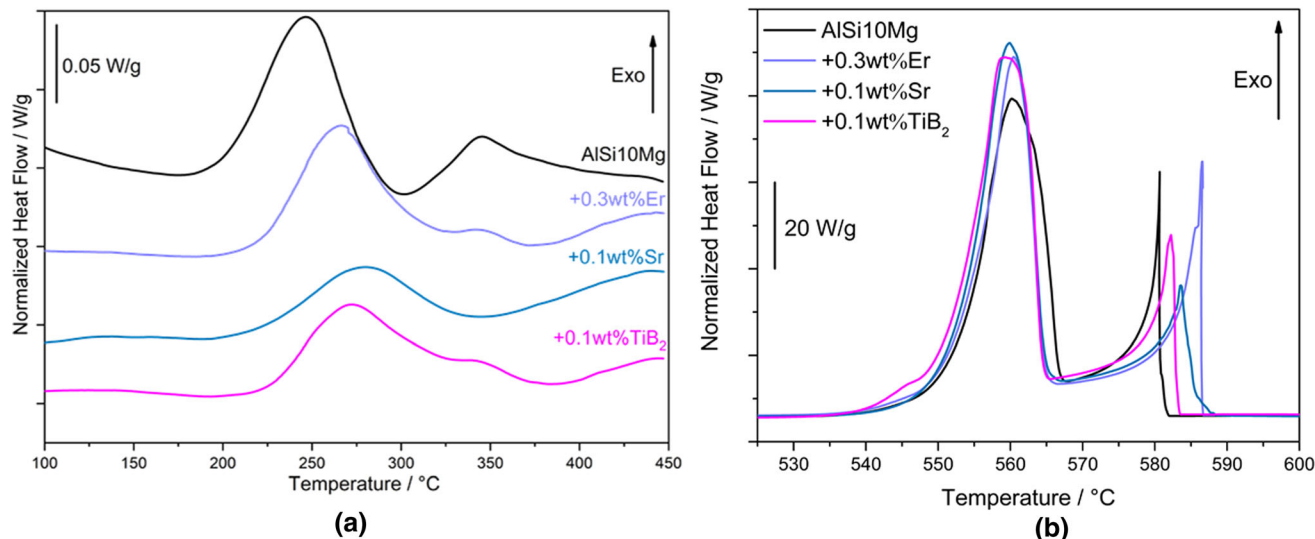
Fig. 5—Comparison of the precipitation signals (*a*) and the solidification curves (*b*) observed in the melt-spun samples of AlSi10Mg and AlSi10Mg containing Er, Sr, and nano-TiB$_2$.

Table IV. Onset Temperatures and Precipitation Enthalpies for the Unmodified AlSi10Mg Alloy and the Alloys Modified with 0.3 Wt Pct Er, 0.1 Wt Pct Sr, and 0.1 Wt Pct Nano-TiB$_2$

	T_{onset} (°C) Cooling	ΔH_{sol} (J/g)
AlSi10Mg	197 ± 1	17 ± 1
AlSi10Mg + Er	219 ± 1	15 ± 1
AlSi10Mg + Sr	216 ± 1	7 ± 1
AlSi10Mg + TiB$_2$	224 ± 1	12 ± 1

the findings of an interaction of the modifiers with the potential nucleation sites of eutectic Si.[21,25,27,48]

Finally, investigations were carried out to evaluate how the eutectic modification by inoculants affects the alloys hardness. Table V reports the results of nano-indentation measurements performed on the cross-section of the ribbons.

All modified alloys have lower hardness than AlSi10Mg in the as-spun condition. This decrement can be associated mainly to the morphological changes of eutectic Si. The continuous Si network is responsible for the increased mechanical properties of Al–Si alloys obtained after RS, as demonstrated in the literature.[14,15] The loss of this network in favor of isolated Si particles of larger size and dispersed in the matrix causes worsening of hardness and yield strength and a ductility increase.[15] The same effect was observed after thermal treatment of Al–Si alloys. It is believed that the slightly reduced hardness values obtained for the modified ribbons are related to a decrease in solid solution strengthening and the less efficient blocking of dislocations provided by the Si crystals, while the strengthening related to grain refinement remains unchanged.

Nevertheless, the presence of fine but more homogeneously dispersed Si particles could improve the mechanical properties of additively manufactured AlSi10Mg samples even in the as-built condition.

IV. CONCLUSIONS

The modification of AlSi10Mg with Er, Sr, and nano-TiB$_2$ leads to several effects. All additions provided limited undercooling for the crystallization of α-Al, but enhanced the undercooling for eutectic Si crystallization. The combination of these two phenomena results in the peculiar microstructures observed in the ribbons, *i.e.*, Si network is less continuous, although finer with Er and Sr, and disrupted with several Si crystals dispersed in the matrix with nano-TiB$_2$. Moreover, considering that all the ribbons have approximately the same Al grains width, it seems that Al nucleation is similar and that RS is the main responsible for Al grains refinement.

Nevertheless, modifiers have different effects on eutectic Si solidification. When adding Er, Si supersaturation is of the same order of magnitude as the base alloy, but Si crystals in the microstructure are larger than in AlSi10Mg. This suggests a decrease in nucleation frequency of eutectic Si due to the formation of poisonous species in the interdendritic liquid.

In the Sr-containing alloy, Si crystallites are alike those of AlSi10Mg, but supersaturation is the lowest, indicating that nucleation of eutectic Si at higher undercooling is favored.

The lack of Al grain refinement in the nano-TiB$_2$ ribbon is probably due to the poisonous interaction between TiB$_2$ and TiAl$_3$ and solute Si. The distribution of Si in rows perpendicular to the ribbon cross-section at the wheel side confirms this harmful interaction. It is deduced that Ti-rich particles and solute Si are rejected from the Al matrix in the interdendritic melt. Here, Ti-rich particles act as heterogeneous nucleation sites for Si, leading to larger Si crystals.

In all modified ribbons, the nano-indentation hardness was lower than in the AlSi10Mg one showing the effect of the continuous eutectic Si network on it. However, the interrupted eutectic Si network could lead

Table V.   Comparison of the Hardness Values Measured on the Cross-Section of the Unmodified and Modified Ribbons Through Nano-indentation

	AlSi10Mg	AlSi10Mg + Er	AlSi10Mg + Sr	AlSi10Mg + TiB$_2$
Hardness (GPa)	1.8 ± 0.3 [23]	1.5 ± 0.3	1.3 ± 0.5	1.1 ± 0.4

to a more homogeneous Si distribution inside bulk samples produced by AM, making mechanical properties more isotropic.

CONFLICT OF INTEREST

On behalf of all authors, the corresponding author states that there is no conflict of interest.

REFERENCES

1. R. Meharabian, B.H. Kear, and M. Cohen: in *Rapid Solidification Processing, Principles and Technologies*. R. Meharabian, B.H. Kear, and M. Cohen, eds., Claitor's Publishing Division, Reston, VA, 1980, pp. 1–23.
2. B.H. Kear, B.C. Giessen, and M. Cohen: in *Proceedings of the Materials Research Society Annual Meeting*. B.H. Kear, B.C. Giessen, and M. Cohen, eds., Elsevier Science Publishing Co., Boston, MA, 1981.
3. H. Liebermann: *Rapidly Solidified Alloys*, Maecrel Dekker, Inc., New York, NY, 1993.
4. S. Steeb and H. Warlimont: in *Proceedings of the Fifth International Conference on Rapidly Quenched Metals*. S. Steeb and H. Warlimont, eds., North-Holland Physics Publishing, Wurzburg, 1984.
5. R. Trivedi, F. Jin, and I.E. Anderson: *Acta Mater.*, 2003, vol. 51, pp. 289–300.
6. Z. Chen, Y. Lei, and H. Zhang: *JALCOM*, 2011, vol. 509, pp. 7473–77.
7. A. Bendijk, R. Delhez, L. Katgerman, Th.H. De Keijser, E.J. Mittemeijer, and N.M. Van Der Pers: *J. Mater. Sci.*, 1980, vol. 15, pp. 2803–10.
8. H.J. Hegge and JTh.M. De Hosson: *Scripta Metall. Mater.*, 1990, vol. 24, pp. 593–99.
9. T. DebRoy, H.L.L. Wei, J.S.S. Zuback, T. Mukherjee, J.W.W. Elmer, J.O.O. Milewski, A.M.M. Beese, A. Wilson-Heid, A. De, and W. Zhang: *Prog. Mater. Sci.*, 2018, vol. 92, pp. 112–224.
10. M. Tang, P.C. Pistorius, S. Narra, and J.L. Beuth: *JOM*, 2016, vol. 68, pp. 960–66.
11. S. Marola, D. Manfredi, G. Fiore, M.G. Poletti, M. Lombardi, P. Fino, and L. Battezzati: *JALCOM*, 2018, vol. 742, pp. 271–79.
12. T. Maeshima and K. Ohishi: *Heliyon*, 2019, vol. 5, p. e01186.
13. H. Qin, Q. Dong, V. Fallah, and M.R. Daymond: *Metall. Mater. Trans. A*, 2020, vol. 51A, pp. 448–66.
14. K.G. Prashanth, S. Scudino, H.J. Klauss, K.B. Surreddi, L. Löber, Z. Wang, A.K. Chaubey, U. Kühn, and J. Eckert: *Mater. Sci. Eng. A*, 2014, vol. 590, pp. 153–60.
15. W. Li, S. Li, J. Liu, A. Zhang, Y. Zhou, Q. Wei, C. Yan, and Y. Shi: *Mater. Sci. Eng. A*, 2016, vol. 663, pp. 116–25.
16. J.H. Martin, B.D. Yahata, J.M. Hundley, J.A. Mayer, T.A. Schaedler, and T.M. Pollock: *Nature*, 2017, vol. 549, pp. 365–69.
17. L. Thijs, K. Kempen, J.P. Kruth, and J. Van Humbeeck: *Acta Mater.*, 2013, vol. 61, pp. 1809–19.
18. R.S. Rana, R. Purohit, and S. Das: *Int. J. Sci. Res. Publ.*, 2012, vol. 2, pp. 1–7.
19. A. Knuutinen, K. Nogita, S.D. McDonald, and A.K. Dahle: *J. Light Met.*, 2001, vol. 1, pp. 229–40.
20. P.S. Mohanty and J.E. Gruzleski: *Acta Mater.*, 1996, vol. 44, pp. 3749–760.
21. S. Hegde and K.N. Prabhu: *J. Mater. Sci.*, 2008, vol. 43, pp. 3009–21.
22. F. Belelli, R. Casati, M. Riccio, A. Rizzi, M.Y. Kayacan, and M. Vedani: *Metals*, 2021, vol. 11, pp. 35–48.
23. S. Marola, D. Gianoglio, F. Bosio, A. Aversa, M. Lorusso, D. Manfredi, M. Lombardi, and L. Battezzati: *JALCOM*, 2020, vol. 821, p. 153538.
24. X. Hu, F. Jiang, F. Ai, and H. Yan: *JALCOM*, 2012, vol. 538, pp. 21–27.
25. P. Pandee, U. Patakham, and C. Limmaneevichitr: *JALCOM*, 2017, vol. 728, pp. 844–53.
26. D. Gianoglio, S. Marola, L. Battezzati, A. Aversa, F. Bosio, M. Lombardi, D. Manfredi, and M. Lorusso: *Intermetallics*, 2020, vol. 119, p. 106724.
27. H. Liao, Y. Sun, and G. Sun: *Mater. Sci. Eng. A*, 2002, vol. 335, pp. 62–66.
28. A.M.A. Mohamed, F.H. Samuel, A.M. Samuel, and H.W. Doty: *Mater. Des.*, 2009, vol. 30, pp. 4218–29.
29. X. Liu, Y. Zhang, B. Beausir, F. Liu, C. Esling, F. Yu, X. Zhao, and L. Zuo: *Acta Mater.*, 2015, vol. 97, pp. 338–47.
30. A.L. Greer, P.S. Cooper, M.W. Meredith, W. Schneider, P. Schumacher, J.A. Spittle, and A. Tronche: *Adv. Eng. Mater.*, 2003, vol. 5, pp. 81–91.
31. E. Samuel, B. Golbahar, A.M. Samuel, H.W. Doty, S. Valtierra, and F.H. Samuel: *Mater. Des.*, 2014, vol. 56, pp. 468–79.
32. C.A. Biffi, P. Bassani, J. Fiocchi, M. Albu, and A. Tuissi: *Mater. Des.*, 2021, vol. 204, p. 109628.
33. V. Raghavan: *JPED*, 2010, vol. 31, pp. 44–45.
34. W. Yi, J. Gao, Y. Tang, and L. Zhang: *CALPHAD: Comput. Coupling Phase Diagr. Thermochem.*, 2020, vol. 68, p. 101732.
35. O. Dezellus, B. Gardiola, J. Andrieux, M. Lomello-Tafin, and J.C. Viala: *JPED*, 2014, vol. 35, pp. 137–45.

36. M. Fass, D. Itzhak, D. Eliezer, and F.H. Froes: *J. Mater. Sci. Lett.*, 1987, vol. 6, pp. 12–13.
37. H. Liao, M. Zhang, Q. Wu, H. Wang, and G. Sun: *Scripta Mater.*, 2007, vol. 57, pp. 1121–24.
38. S. Moniri, X. Xiao, and A.J. Shahani: *Sci. Rep.*, 2019, vol. 9, pp. 40455–63.
39. D. Carluccio, M.J. Bermingham, Y. Zhang, D.H. StJohn, K. Yang, P.A. Rometsch, X. Wu, and M.S. Dargusch: *J. Manuf. Process.*, 2018, vol. 35, pp. 715–20.
40. D. Qiu, J.A. Taylor, M.X. Zhang, and P.M. Kelly: *Acta Mater.*, 2007, vol. 55, pp. 1447–56.
41. R. Delhez, T.H. De Keijser, E.J. Mittemeijer, P. Van Mourik, N.M. Van Der Pers, L. Katgerman, and W.E. Zalm: *J. Mater. Sci.*, 1982, vol. 17, pp. 2887–94.
42. P. Todeschini, G. Champier, and F.H. Samuel: *J. Mater. Sci.*, 1992, vol. 27, pp. 3539–51.
43. S. Moniri and A.J. Shahani: *J. Mater. Res.*, 2019, vol. 34, pp. 20–34.
44. P. Van Mourik, E.J. Mittemeijer, and T.H. De Keijser: *J. Mater. Sci.*, 1983, vol. 18, pp. 2706–20.
45. P. Van Mourik, Th.H. De Keijser, and E.J. Mittemeijer: in *Rapidly Quenched Metals*. S. Steeb and H. Warlimont, eds., Elsevier Science Publishers B.V., Amsterdam, 1985, pp. 899–902.
46. Y. Zhang, H. Zheng, Y. Liu, L. Shi, R. Xu, and X. Tian: *Acta Mater.*, 2014, vol. 70, pp. 162–73.
47. E. Vandersluis, D. Sediako, C. Ravindran, A. Elsayed, and G. Byczynski: *JALCOM*, 2018, vol. 736, pp. 172–80.
48. M. Timpel, N. Wanderka, R. Grothausmann, and J. Banhart: *JALCOM*, 2013, vol. 558, pp. 18–25.